Ultraslow-spread lithosphere accreted by episodic magmatism and serpentinized mantle exhumation

Ingo Grevemeyer (1), Nicholas W. Hayman (2), Christine Peirce (3), Michaela Schwardt (4), Harm J. A. van Avendonk (2), Anke Dannowski (1), and Cord Papenberg (1)

(1) GEOMAR Helmholtz Centre for Ocean Research, Kiel, Germany

(2) Institute for Geophysics, Jackson School of Geosciences, University of Texas, Austin, U.S.A.

(3) Department of Earth Sciences, Durham University, Durham, U.K.

(4) Institute of Geoscience, Christian-Albrechts University, Kiel, Germany

Mid-ocean ridges spreading at ultraslow rates of <20 mm yr^{-1} can exhume serpentinized mantle to the seafloor, or they can produce magmatic crust. However, seismic imaging of ultraslow spreading centres has not been able to resolve the abundance of serpentinized mantle exhumation, and instead supports 2-5 km of crust. Most seismic crustal thickness estimates reflect the depth at which the 7.1 km s^{-1} P-wave velocity is exceeded. Yet, the true nature of the oceanic lithosphere is more reliably deduced using the P- to S-wave velocity (Vp/Vs) ratio. Here, we report on seismic data acquired along off-axis profiles of older oceanic lithosphere at the ultraslow spreading Mid-Cayman Spreading Centre. High Vp/Vs ratios of >1.9 and continuously increasing P-wave velocity, changing from 4 km s^{-1} at the seafloor to >7.4 km s^{-1} at 2 to 4 km depth, indicate highly serpentinized peridotite exhumed to the seafloor. Elsewhere, either magmatic crust or serpentinized mantle deformed and uplifted at oceanic core complexes underlies areas of high bathymetry. The Cayman Trough provides therefore a window into mid-ocean ridge dynamics that switch between magma-rich and magma-poor oceanic crustal accretion, including exhumation of serpentinized mantle to ~25% of the seafloor.

About 60% of the Earth's surface is oceanic crust and new seafloor is continually created along the ~65,000 km long mid-ocean ridge (MOR) system[1]. Most oceanic crust has a relatively uniform thickness, but for about 25% of MORs that spread at an ultraslow spreading rate of <20 mm yr^{-1} melt supply to the ridge is thought to dramatically decrease, implying that crustal thickness should also decrease[2]. The few existing seismic studies of ultraslow spreading MORs undertaken to date reveal that crustal thickness is indeed thin (2-5 km)[2,3,4] when compared to normal oceanic crust formed at slow to fast spreading rates (6-7 km)[5]. However, crust formed at ultraslow spreading rates is also highly diverse in its thickness, structure, and geological composition. For example, both the Gakkel Ridge and Southwest Indian Ridge (SWIR) have areas of enhanced volcanism and other areas where magma-starved conditions promote exhumation of the mantle[6, 7, 8] . Yet, seismic data, which could provide a more complete view of the oceanic lithospheric structure and composition, finds little evidence for magma-poor lithospheric accretion at any spreading rate[3, 4, 5], except in some large massifs, or oceanic core complexes (OCCs), where large-scale detachment faulting[9] exposes upper mantle rocks at the seafloor[10]. However, many OCCs at both slow- and ultraslow spreading rates comprise thick lower crustal sections [11, 12].

Seismic Imaging of Oceanic Lithosphere

Seismic surveys of the oceanic lithosphere find that it is generally formed via continuous magmatic accretion resulting in a well-stratified crust with seismic layers 2 and 3 above the seismic Moho[13, 14]. A widely accepted model[13] equates these seismic layers with an extrusive basaltic upper crust and sheeted dyke complex (layer 2), a gabbroic lower crust (layer 3), and a well-defined crust-mantle boundary. This layered seismic velocity structure and measure crustal thickness should be greatly affected during magma-poor seafloor spreading as mantle is exposed to seawater and serpentinization occurs. In marine seismic studies, crustal thickness is best defined when wide-angle reflections from the seismic Moho are observed along reversed profiles. Alternatively, estimates may be based on the depth at which the P-wave velocity exceeds 7.1-7.2 km s^{-1} [(3, 14, 15)]. Seismically, the upper oceanic crust exhibits a strong velocity gradient with velocities increasing from <4.0 km s^{-1} at the seafloor to ~6.7 km s^{-1} at 1.5-2.0 km depth, while the lower crust exhibits a moderate gradient and velocities of ~6.8 to 7.1 km s^{-1}[(13, 14, 15)]. In contrast, exhumed serpentinized mantle will have a P-wave velocity that increases gradually from ~4 km s^{-1} at the seabed to ~8 km s^{-1} at depth[16, 17, 20]. Thus, most P-wave estimates only discriminate between magmatic oceanic crust and serpentinized mantle exhumed to shallower depths via contrasts in velocity gradients, which is likely insufficient for distinguishing between types of oceanic crust. However, serpentinites are characterized by high P- to S-wave velocity (Vp/Vs) ratios of ≥1.9, compared to 1.75-1.85 in crustal rocks[18, 19] and so this ratio may more reliably provide a tool with which to evaluate the degree of serpentinization in the lithosphere as a whole[16, 18, 20]. Most seismic imaging efforts along ultraslow spreading centres have not, in general, favoured the recording of S-waves for a variety of reasons, not least of which is the lack of sediment cover hindering seismic energy conversion, and instrument coupling to the seafloor.

Diversity of Ultraslow-Spreading Oceanic Lithosphere in the Cayman Trough

The Mid-Cayman Spreading Center (MCSC) (Fig. 1), with its end-member ultraslow spreading rate of ~15 mm yr^{-1}[(21)], not only provides an opportunity to investigate the change from magmatic accretion to amagmatic extension over time, it also allows appraisal of the degree of serpentinization associated with the transition between the magmatic and amagmatic end-member styles of spreading.

Magnetic anomalies suggest that the MCSC has been spreading for at least 45 Myr[(22)]. Its great axial depth (5000-6000 m) and low mantle potential temperature, derived from basalt geochemical signatures, imply that the lithosphere formed from a relatively cold mantle and with a low extent of melting[23]. The bathymetry of the MCSC includes many OCCs (Fig. 1) that differ from those observed on the Mid-Atlantic Ridge [9,21]in their gross morphology, but exhibit many of the same features including mixtures of gabbroic lower crustal and peridotitic mantle rocks exhumed along detachment faults[21]. The central OCC, Mt. Dent, hosts a hydrothermal vent[24] in exhumed, predominantly crustal material where fluids cycle through a deep, mafic crustal root[25]. In the deeper parts of the MCSC to the north and south of Mt. Dent, basalt flows overlie zones of thin crust and, potentially, zones of partial melt[26] that drive the world's deepest known MOR black smoker system located at the northern end of the ridge[24]. However, even in the axial region where upper crustal basalts and lower crustal gabbros are found, serpentinized mantle peridotites are common[21].

Off-axis in the Cayman Trough, in water depths up to 4000 m, seafloor younger than ~10 Ma also hosts many bathymetric highs which we interpret to be OCCs that were internally faulted and deformed, best exemplified by the massif imaged in profile P06. However, for crust older than 10 Ma, the seafloor is much smoother and deeper (>~4500 m).

Seismic Signatures of Serpentinized Mantle and Magmatic Crust

To investigate the extent of exhumed mantle and degree of serpentinization, and determine the true crustal thickness associated with the variation between the different modes of ultraslow seafloor spreading, we report the results of a wide-angle seismic survey that sampled 4-20 Ma crust along a flowline crossing both conjugate MCSC ridge flanks. The profile, comprising two 90 to 110 km long parts encompassing the similarly aged east and west flanks spread from the axis, was instrumented with ocean-bottom seismographs (OBSs) and hydrophones (OBHs) spaced 2-7 km apart. A large tuned seismic source and dense receiver coverage resulted in excellent data quality, recording both P-wave onsets and P-to-S converted arrivals, representing S-waves turning throughout the crust and uppermost mantle. Crustal phases (Pg, Sg) are ubiquitous and, between 10-60 km offset, mantle arrivals (Pn, Sn) are observed with fast apparent Pn velocities of >7.5 km s^{-1}. Travel-time picks of these phases were tomographically inverted (see Methods) to reveal the detailed crustal structure (Fig. 2).

Our modelling shows that the western ridge flank has lateral (temporal) changes in velocity structure that we correlate with lithological variations associated with varying degrees of magmatism and mantle exhumation (Fig. 3). For lithosphere older than ~10 Ma, both P- and S-wave velocities show a laterally uniform and continuous increase with depth, with the P-wave velocity increasing from 4.0 to ~7.4 km s^{-1} and a Vp/Vs ratio >1.9. Seafloor younger than ~10 Ma shallows to <4000 m and the velocity-depth structure is more reminiscent of the layer 2-layer 3-type structure of magmatically accreted oceanic crust[15] with corresponding Vp/Vs ratios of <1.9. Using the 7.1 km s^{-1} P-wave velocity contour as indicative of the crust/mantle boundary, since the inversion approach will not generate a well-defined velocity discontinuity, and defining the mantle as having a velocity of >7.4 km s^{-1}, crustal thickness is estimated to be 3-5 km to the west of the MCSC. Thus, phases of both magmatic accretion and exhumation of serpentinized mantle occurred, each lasting on the order of ~2 Myr. The change from magmatic to amagmatic seismic structure at ~70 km from the MCSC is supported by the gravity anomaly, which has been interpreted[27] to reflect a change of crustal thickness at ∼10 Ma. Our results suggest that the gravity low reflects exhumed and serpentinized mantle (see Methods). We interpret the 2-3 km domain sub-seabed as exhumed mantle similar to that observed at magma poor margins[16,17,20].

About 50 km to the west of the ridge axis a dome-like structure shallows to ~2500 m water depth and exhibits high Vp/Vs ratios along its eastern ridge-dipping flank. We interpret this dome as a fossil OCC with upper mantle material exposed by detachment faulting given the corresponding Vp/Vs ratios. Except for the core complex, the eastern conjugate ridge flank mimics the features of the western flank, although there is a distinct asymmetry in the durations of periods of magmatic vs amagmatic spreading. However, the pattern of high-low Vp/Vs ratio is more chaotic than on the western flank and, based on studies in other regions[28,29], is interpreted as resulting from the intrusion of gabbroic melts into the mantle, and thus OCC footwalls tend to spread to the west relative to their hanging walls[21]. The high degree of heterogeneity observed in this off-axis setting is also observed by P-wave seismic data collected along the MCSC and across the Mt. Dent hydrothermal vent field, revealing both domains of volcanic seafloor and un-roofed mantle[25,26], though in those instances the lack of Vs arrivals permits alternative interpretations of the abundance of magmatism relative to serpentinization.

A Local and Global Estimate of Serpentinized Mantle Abundance

Using the Vp/Vs=1.9 to discriminate between serpentinized mantle (≥1.9) and magmatically accreted crust (<1.9) (see Methods), we observe that along our profile 25% of the western flank and 20% of the eastern flank, respectively, have a Vp/Vs > 1.9, suggesting that serpentine is abundant and in many places exposed at the seafloor. In contrast, crust and mantle formed at fast[16] and slow[30] spreading rates are comparatively uniform and do not support Vp/Vs ratios >1.9 (Fig. 4). Many of the domains of high Vp/Vs ratio occur in the deeper, smoother >10-Ma-old seafloor. Other domains of high Vp/Vs occur within the rougher seafloor, such as the axial-dipping zone atop the deformed OCC in profile P06, which is otherwise underlain by crustal materials. Thus, mantle exhumation during MCSC seafloor spreading occurs both during OCC formation in association with exhumation of thicker crustal sections[25], but also through continuous un-roofing of the mantle. The latter, continuous mode of mantle exhumation is further characterized by seafloor that is well below the depth expected from the plate cooling trend[22, 27] and, hence, is also marked by a depth anomaly of 500-1000 m.

The diversity of seafloor types, and especially the deep seafloor regions in the Cayman Trough strongly resemble smooth domains of other ultraslow spreading centres, such as the SWIR[8] where predominantly exhumed, serpentinized mantle is thought to dominate, punctuated by local basalt flows and OCCs of thick lower crustal sections[12]. Ultraslow spreading centres themselves reflect a quarter of the global ridge length[1, 6], and many of the mantle exhumation and serpentinization processes that occur along them are observed along other plate-boundary systems. There are key geochemical fluxes and biological activity associated with serpentinization[31], yet scientific drilling and seafloor geologic mapping have not been able to produce robust measures of the amount of serpentinization along slower spreading centres[32]. Extrapolating from our data from the Cayman

Trough to other localities such as the SWIR and Gakkel Ridge, we estimate that ultraslow spreading centres accrete lithosphere that is up to 25% serpentinized mantle, placing a possible bound on the long-term serpentinization of ultraslow spreading centres worldwide.

Evolution from Magma-Poor to Magma-Rich Seafloor Spreading

Our geophysical observations from the Cayman Trough indicate that there are 2-10 Myr temporal variations in seafloor morphology and abundant Vp/Vs anomalies (Fig. 4). Though limited to a ~15-20 Myr history of seafloor spreading, our data also suggest that there is an evolution along the imaged flow line from relatively deep seafloor dominated by magma poor spreading conditions and serpentinized mantle, to more complexly faulted mixtures of lower crust and serpentinized mantle. The latter, more recent style of seafloor spreading, including OCC formation, typifies the active spreading centre where two areas of basaltic lavas bound regions of exhumed lower crust and serpentinized mantle. A similar structure is observed along the SWIR and much of the slow-spreading Mid-Atlantic Ridge where OCCs are thought to be indicative of mixed amounts of magmatic and tectonic extension[33]. One explanation for the abundance of magma-poor ultraslow-spreading mid-ocean ridges is that passive mantle upwelling dominates over buoyant upwelling at rates <20 mm yr^{-1} [(6)]. The diversity of the Cayman Trough lithosphere indicates that mantle upwelling can occur through either process at rates <20 mm yr^{-1} resulting in serpentinized mantle exhumation during some geologic time intervals, and delivering melt to the crust during others.

References

1 R. Searle (2013), Mid-Ocean Ridges, Cambridge University Press, ISBN-13: 978-1107017528, pp 330.

2 White, R.S., T.A. Minshull, M. Bickle, and C.J. Robinson (2001), Melt generation at very slow-spreading oceanic ridges: constraints from geochemical and geophysical data, J. Petrol., 42, 1171–1196.

3 Jokat, W., and M. C. Schmidt-Aursch (2007), Geophysical characteristics of the ultraslow spreading Gakkel Ridge, Arctic Ocean, Geophys. J. Int., 168(3), 983–998, doi:10.1111/j.1365-246X.2006.03278.x.

4 Minshull, T. A., M. R. Muller, and R. S. White (2006), Crustal structure of the Southwest Indian Ridge at 66°E: Seismic constraints, Geophys. J. Int., 166, 135–147, doi:10.1111/j.1365-246X.2006.03001.x.

5 van Avendonk, H.J.A., J.K. Davis, J.L., Harding, and L.A. Lawver (2017), Decrease in oceanic crustal thickness since the breakup of Pangaea, Nat. Geosci., 10(1), 58-62, doi:10.1038/NGEO2849.

6 Dick et al. (2003), An ultraslow-spreading class of ocean ridge, Nature 426, 405-412.

7 Michael et al. (2003), Magmatic and amagmatic seafloor generation at the ultraslow spreading Gakkel Ridge, Arctic Ocean, Nature, 423, 956-961.

8 Sauter, D., et al. (2013), Continuous exhumation of mantle-derived rocks at the Southwest Indian Ridge for 11 million years, Nat. Geosci., 6(4), 314–320, doi:10.1038/ngeo1771.

9 Smith, D. K., J. R. Cann, and J. Escartin (2006), Widespread active detachment faulting and core complex formation near 13°N on the Mid-Atlantic Ridge, Nature, 442, 440–443, doi:10.1038/nature04950.

10 Canales, J. P., B. E. Tucholke, M. Xu, J. A. Collins, and D. L. DuBois (2008), Seismic evidence for large-scale compositional heterogeneity of oceanic core complexes, Geochem. Geophys. Geosyst., 9, Q08002, doi:10.1029/2008GC002009.

11 Blackman, D. K., et al. (2011), Drilling constraints on lithospheric accretion and evolution at Atlantis Massif, Mid-Atlantic Ridge 30°N, J. Geophys. Res., 116, B07103, doi:10.1029/2010JB007931.

12 Dick, H. J. B., et al. (2000), A Long In-Situ Section of the Lower Ocean Crust: Results of ODP Leg 176 Drilling at the Southwest Indian Ridge, Earth Planet. Sci., 179, 31–51, doi:10.1016/S0012-821X(00)00102-3.

13 White, R. S., D. McKenzie, and R. K. O'Nions (1992), Oceanic crustal thickness from seismic measurements and rare earth element inversions, J. Geophys. Res., 97, 19,683– 19,715.

14 Grevemeyer, I., C.R. Ranero, and M. Ivandic (2017), Structure of oceanic crust and serpentinization at subduction trenches, Geosphere, 14, doi:10.1130/GES01537.1.

15 Carlson, R. L., and D. Jay Miller (2004), Influence of pressure and mineralogy on seismic velocities in oceanic gabbros: Implications for the composition and state of the lower oceanic crust, J. Geophys. Res., 109, B09205, doi:10.1029/2003JB002699.

16 Prada, M., V. Sallares, C.R. Ranero, M.G. Vendrell, N. Zitellini, I. Grevemeyer (2016), Mantle exhumation and sequence of magmatic events in the Magnaghi–Vavilov Basin (Central Tyrrhenian, Italy): New constraints from geological and geophysical observations, Tectonophysics 689, 133–142, doi:10.1016/j.tecto.2016.01.041

17 Dean, S. M., T. A. Minshull, R. B. Whitmarsh, and K. E. Louden (2000), Deep structure of the ocean-continent transition in the southern Iberia abyssal plain from seismic refraction profiles: The IAM-9 transect at 40°20'N, J. Geophys. Res., 105(B3), 5859–5885.

18 Christensen, N. I. (2004), Serpentinites, peridotites, and seismology, Int. Geol. Rev., 46, 795–816, doi:10.2747/0020-6814.46.9.795.

19 Carlson, R. L., and D. J. Miller (1997), A new assessment of the abundance of serpentinite in the oceanic crust, Geophys. Res. Lett., 24, 457-460.

20 Bullock, A. D. and Minshull, T. A. (2005), From continental extension to seafloor spreading: crustal structure of the Goban Spur rifted margin, southwest of the UK, Geophys. J. Int., 163, 527–546. doi:10.1111/j.1365-246X.2005.02726.x

21 Hayman, N. W., N. R. Grindlay, M. R. Perfit, P. Mann, S. Leroy, and B. M. de Lépinay (2011), Oceanic core complex development at the ultraslow spreading Mid-Cayman Spreading Centre, Geochem. Geophys. Geosyst., 12, Q0AG02, doi:10.1029/2010GC003240.

22 Rosencrantz, E., R. I. Malcom, and J. G. Sclater (1988), Age and spreading history of the Cayman trough as determined from depth, heat flow, and magnetic anomalies, J. Geophys. Res., 93, 2141–2157, doi:10.1029/JB093iB03p02141

23 Klein, E. M., and C. H. Langmuir (1987), Global correlations of ocean ridge basalt chemistry with axial depth and crustal thickness, J. Geophys. Res., 92, 8089–8115, doi:10.1029/JB092iB08p08089.

24 Connelly, D.P., et al., (2012), Hydrothermal vent fields and chemosynthetic biota on the world's deepest seafloor spreading centre. Nat. Commun. 3, doi:10.1038/ncomms1636.

25 Harding, J.L., H. J.A., van Avendonk, N.W. Hayman, I.Grevemeyer, C. Peirce, and A. Dannowski (2017), Magmatic-tectonic condictions for hydrothermal venting on an ultraslow-spread oceanic core ceomplex, Geology, 45, 839-842, doi: 10.1130/G39045.1

26 Van Avendonk, H.J.A., N.W. Hayman, J.L. Harding, I. Grevemeyer, C. Peirce, and A. Dannowski (2017), Seismic structure and segmentation of the axial valley of the Mid-Cayman Spreading Centre, Geochem. Geophys. Geosyst., 18, 2149–2161, doi:10.1002/2017GC006873.

27 ten Brink, U., D. Coleman, and W. P. Dillon (2002), The nature of the crust under Cayman trough from gravity, Mar. Pet. Geol., 19, 971–987, doi:10.1016/S0264-8172(02)00132-0.

28 Cannat, M., et al. (1995), Thin crust, ultramafic exposures, and rugged faulting patterns at the Mid-Atlantic Ridge (22°–24°N), Geology, 23, 49–52, doi:10.1130/0091-613(1995)023<0049:TCUEAR>2.3.CO;2.

29 Lizarralde, D., J.B. Gaherty, J.A. Collins, G. Hirth, and S.D. Kim (2004), Spreading-rate dependence of melt extraction at mid-ocean ridges from mantle refraction data, Nature, 432, doi:10.1038/nature03140, 744-747.

30 Dannowski, A., I. Grevemeyer, J. Phipps Morgan, C. R. Ranero, M. Maia, and G. Klein (2011), Crustal structure of the propagating TAMMAR ridge segment on the Mid-Atlantic Ridge, 21.5°N, Geochem. Geophys. Geosyst., 12, Q07012, doi:10.1029/2011GC003534.

31 Früh-Green, G.L., J.A.D. Connolly, A. Plas, D.S. Kelley, and B. Grobety (2004), Serpentinization of oceanic peridotites: implications for geochemical cycles and biological activity, Geophysical Monograph, 114, 119-136.

32 Cannat, M., F. J. Fontaine, and J. Escartín (2010), Serpentinization and associated hydrogen and methane fluxes at slow spreading ridges, in Diversity of Hydrothermal Systems on Slow Spreading Ocean Ridges, edited by P. A. Rona et al., pp. 241–263, AGU, Washington, D. C.

33 Olive, J.-A., M. D. Behn, and B. E. Tucholke (2010), The structure of oceanic core complexes controlled by the depth distribution of magma emplacement, Nat. Geosci., 3, 491–495, doi:10.1038/NGEO888.

Acknowledgements

Funding for this project was obtained from the German Science Foundation (DFG), supporting RV METEOR cruise M115, from the U.S. National Science Foundation (NSF) under grant OCE-1356895, and from the British Natural Environment Research Council (NERC) under grant NE/K011162/1.

Authors thank the captain, officers and crew of RV METEOR for their assistance during the CAYSEIS cruise.

Author Contributions

I.G., N.W.H., H.J.A.V.A., C.P. and A.D. planned the survey and obtained the funding. All co-authors contributed in collecting the data at sea and discussed results. C.PA., I.G., and M.S. processed the data. I.G. and M.S. conducted seismic inversions and errors analysis. C.P. conducted the analysis of the gravity data. I.G. N.W.H. and C.P. wrote the paper within input from H.J.A.V.A. and all authors commented on the manuscript.

Figure 1 | Cayman Trough bathymetry and layout of seismic experiment. Location of seismic lines P05 and P06 (solid lines) and ocean-bottom-seismomographs (white circles) sampling ~4 to up to 20 Ma old seafloor. Seafloor age isochrones are approximated by broken lines and ages are given by numbers. Red ellipses indicate bathymetric highs interpreted as oceanic core complexes.

Figure 2 | Seismic results. a) Bathymetry along P06 on the western flank of the MSCS, b) Vp/Vs ratio of P06, c) P-wave velocity model, d) bathymetry along P05 on the eastern flank, e) Vp/Vs ratio of P06, and f) P-wave velocity model.

Figure 3 | P-wave properties of magmatic and amagmatic domains. a) Velocity-depth functions from magmatic domains with Vp/Vs < 1.9 indicating a 1-2 km thick upper crustal formation and a low gradient lower crust, b) areas with Vp/Vs > 1.9 show velocities gradually increasing to values too fast to represent gabbroic crust. Light grey indicates young Atlantic crust[13] and dark grey serpentinized mantle found in the Tyrrhenian Sea[16].

Figure 4 | Vp/Vs ratio as a proxy for rock types and mantle serpentinization. a) Constraints from laboratory studies on P-wave and S-wave velocity of different rocks from mid-ocean ridges (see Methods for data sources), b) field definition to distinguish rocks types, c) results from P06 on the western ridge flank of MCSC, d) results from P05 on the eastern ridge flank of MCSC, e) P-wave and S-wave velocity data from the Mid-Atlantic Ridge[30], and f) from crust formed at the East Pacific Rise[14].

Methods

Data acquisition: Seismic data were acquired in April 2015 in the Cayman Trough aboard the German research vessel METEOR. Two profiles were shot surveying mature lithosphere across both ridge flanks of the Mid-Cayman Spreading Centre. Profile P05, 105 km long, sampled the eastern ridge flank, covering 4 to 20 Myr old seafloor[21, 34]. In total, 26 ocean-bottom seismographs from GEOMAR, UTIG, and the UK Ocean-Bottom Instrumentation Facility[35] were deployed at 2 to 5 km spacing. P06, 90 km long, investigated 4 to 14 Myr old lithosphere[21, 34] of the conjugated western flank. Due to limited time at the end of the survey, the profile had a larger instrument spacing of 7.5 km between nine OBS. As seismic source we used a tuned airgun array with a total volume of 86 litres fired at a pressure of 210 bars. All OBS recorded both P-wave and S-wave arrivals (SI Figs 1 and 2) and neither P-waves nor S-waves provided any evidence for a well-defined crust/mantle boundary. However, large offsets of up to 80 km and apparent velocities of 7.8 to 8.0 kms^{-1} suggest that most OBSs recorded energy turning in crust (Pg, Sg) and mantle (Pn, Sn).

Seismic data analysis and inversion: Travel times of first arrival P-waves and secondary arriving S-waves have been hand-picked. In general, picking uncertainties were 20-30 ms for short-offset P-waves (Pg) and reach 40 ms for far-offset P-waves (Pn) and secondary short-offset S-waves (Sg). The largest uncertainties of 60 ms were assigned to far-offset S-wave mantle arrivals (Sn). For profile P05, picking resulted in 14652 P-wave arrival and 5420 S-waves arrival travel times. Profile P06 provided 3698 P-wave and 1395 S-wave travel time picks.

Seismic refraction travel time data were used to derive 2-D velocity models using a seismic tomography approach[36]. The method employs a hybrid ray-tracing scheme combining the graph method with further refinements utilizing ray bending with the conjugate gradients method. Smoothing and damping constraints regularize the iterative inversion. A detailed description of this method is given elsewhere[36]. Picking errors and starting velocity models may control inversion results. We therefore chose a nonlinear Monte Carlo-type error analysis to derive model uncertainties (SI Figs 3 and 4). The approach consists of randomly perturbing the velocity values of an initial average 1-D model to create a set of 100 2-D reference models[37] for both P- and S-waves. Profile P05 provided an rms misfit of 36-48 ms for the P-wave and 49-73 ms for the S-wave inversions. Profile P06 had slightly larger rms misfits of 65-78 ms for the P-wave and 59-120 ms for the S-wave models. For each model, we applied a top-to-bottom layer stripping approach and only five iterations were required to exceed a χ^2 threshold of 1. The mean deviation of all the solutions was then used as a measure of the model parameters uncertainty[38]. The ray coverage of the models is represented by the derivative weight sum (DWS), which is a measure of the linear sensitivity of the inversion[39]. To obtain the uncertainty in the Vp/Vs ratio, we randomly combined the 100 different P-waves and S-waves, obtained Vp/Vs ratios, and calculated the rms error.

Vp/Vs ratio: Any interpretation of P-wave velocity with respect to lithology is tenuous. Generally, crustal material is interpreted to have a velocity of ~4 km s^{-1} at the seafloor[13, 14] increasing to 7.1 km s^{-1} at the base of the oceanic crust[14, 19]. However, serpentinized mantle may have a seismic velocity of 4.5 km s^{-1} for highly serpentinized mantle decreasing to ~8 km s^{-1} for dry mantle[18, 19] a range overlapping with crustal-type velocities. S-wave velocity and hence Vp/Vs ratio can be used to discriminate between different rock types. Both basalts and gabbros generally have Vp/Vs ratios of <1.9 [ref 40-46] while serpentinized mantle generally has much higher Vp/Vs ratios [ref 45-49](Fig. 4a) ranging, for low-temperature alteration and the formation of Lizardite, from ~1.8 for very low degrees of alteration to ratios of >2.1 [ref 18]. Consequently, the Vp/Vs ratio is a useful tool, or proxy, to distinguish mantle and crustal-derived lithology's, when considered in concert with both the P-wave and S-wave velocity lateral and vertical variation within a model space (Fig. 4a).

Gravity data analysis: Gravity data were recorded along all seismic lines using a Lacoste & Romberg Micro-G sea-air gravimeter. The calculated free-air anomaly (FAA) was tied to absolute gravity reference stations in Jamaica and Guadeloupe. For modelling, the seismic tomography P-wave velocity model was converted to a block density model using velocity contours and matching standard velocity-density relationships suited to the oceanic crust (SI Fig. 5), with the FAA in the

127.21 km ridge-axis gap between profiles P05 and P06 derived from satellite altimeter data[50], to enable crustal structure determination for current spreading conditions. The combined ship and satellite FAA was modelled using a polygon approach[51], and only in areas of little ray coverage at model extremities did any seismic model-derived block geometry require adjustment to achieve a good anomaly fit. Individual block density variations across-axis, distinguishable within seismic model velocities resolution, match interpreted patterns of seabed lithology, with magmatic and magma poor periods clearly correlated.

34 Müller, R. D., M. Sdrolias, C. Gaina, and W. R. Roest (2008), Age, spreading rates, and spreading asymmetry of the world's ocean crust, Geochem. Geophys. Geosyst., 9, Q04006, doi:10.1029/2007GC001743.

35 Minshull, T.A.,M.C. Sinha, and C. Peirce (2005), Multi-disciplinary, sub-seabed geophysical imaging: A new pool of 28 seafloor instruments in use by the United Kingdom Ocean Bottom Instrument Consortium: Sea Technology, 46, no. 10, p. 27–31.

36 Korenaga, J., W.S. Holbrook, G.M. Kent, P.B. Kelemen, R.S. Detrick, H.-C. Larsen, J.R. Hopper, and T. Dahl-Jensen (2000), Crustal structure of the southeast Greenland margin from joint refraction and reflection seismic tomography, J. Geophys. Res., 105, 21 591–21 614.

37 Kahle, R.L., F. Tilmann, and I. Grevemeyer (2016), Crustal structure and kinematics of the TAMMAR propagating rift system on the Mid-Atlantic Ridge from seismic refraction and satellite altimetry gravity, Geophys. J. Int., 206(2), 1382–1397, doi:10.1093/gji/ggw219

38 Tarantola, A. (1987), Inverse Problem Theory: Methods for Data Fitting and Model Parameter Estimation, pp. 613, Elsevier Science, New York.

39 Toomey, D. R., and G. R. Foulger (1989), Tomographic inversion of local earthquake data from Hengill-Grensdalur central volcano complex, Iceland, J. Geophys. Res., 94, 17,497–17,510.

40 Johnston, J.E., N.I. Christensen (1997), Seismic properties of layer 2 basalts, Geopys. J. Int., 128, 285-300.

41 Christensen, N.I., W.W. Wepfer, R.D. Baus (1989), Seismic Properties of Sheeted Dikes from Hole 504B, ODP Leg 111, in: Proceedings of the Ocean Drilling Program, Scientific Results, 111, 171-176, doi:10.2973/odp.proc.sr.111.153.1989.

42 Salisbury, M.H., J.H. Scott, C. Aurox, K. Becker, W. Bosum, C. Broglia, R. Carlson, N.I. Christensen, A. Fisher, J. Gieskes, M.A. Holmes, H. Hoskins, D. Moos, R. Stephen, and R. Wilkens (1988), Old Oceanic Crust: Synthesis of Logging, Laboratory, and Seismic Data from Leg 102. In Proceedings of the Ocean Drilling Program, Scientific Results, 102, 155-180, doi:10.2973/odp.proc.sr.102.123.1988.

43 Wilkens, R.H., N.I. Christensen, and L. Slater, High-Pressure Seismic Studies of Leg 69 and 70 Basalts, In Cann, J. R., Langseth, M. G., Honnorez, J., Von Herzen, R. P., White, R. P., et al., Init. Repts. DSDP, 69, Washington (U.S. Govt. Printing Office), 683-686, doi:10.2973/dsdp.proc.69.142, 1983

44 Iturrino, G.J., N.I. Christensen, S. Kirby, and M.H. Salisbury (1991), Seismic velocities and elastic properties of oceanic gabbroic rocks from Hole 735B. In: Proceedings of the Ocean Drilling Programm, Scientific Results, 118, 227-244, doi:10.2973/odp.proc.sr.118.151.1991.

45 Iturrino, G.J., D.J. Miller, and N.I. Christensen (1996), Velocity Behavior of Lower Crustal and Upper Mantle Rocks from a fast-spreading Ridge at Hess Deep. In: Proceedings of the Ocean Drilling Programm, Scientific Results, 147, 417-440, doi:10.2973/odp.proc.sr.147.027.1996.

46 Miller, D.J., and N.I. Christensen (1997), Seismic velocities of lower crustal and upper mantle rocks from the slow spreading Mid-Atlantic Ridge, south of the Kane Tranform Zone (MARK). In: Proceedings of the Ocean Drilling Programm, Scientific Results, 153, 437-454, doi:10.2973/odp.proc.sr.153.043.1997.

47 Christensen N.I. (1966), Elasticity of ultrabasic rocks, J. Geophys. Res., 71.24, 5921-5931.

48 Christensen, N.I. (1972), The abundance of serpentinites in the oceanic crust, J. Geology, 80, 709-719.

49 Christensen N.I. (1978), Ophiolites, seismic velocites and oceanic crustal structure, Tectonophysics, 47, 131-157.

50 Sandwell, D.T., R.D. Müller, W.H.F. Smith, E. Garcia, R. Francis (2014), New global marine gravity model from CryoSat-2 and Jason-1 reveals buried tectonic structure, Science, 346, 6205, 65-67, doi:10.1126/science.1258213.

51 Talwani,M., Worzel,J.L. and Landisman,M. (1959), Rapid gravity computation for two-dimensional bodies with application to the Mendocino Submarine Fracture Zone. J. Geophys. Res., 64, 49-59.

Data availability.

The seismic data used in this study will be made available at the Academic Seismic Portal at UTIG (www-udc.ig.utexas.edu/sdc), the World Data Center PANGAEA (www.pangaea.de), and the British Oceanographic Data Centre (www.bodc.ac.uk) or can be requested from I.G. (igrevemeyer@geomar.de).

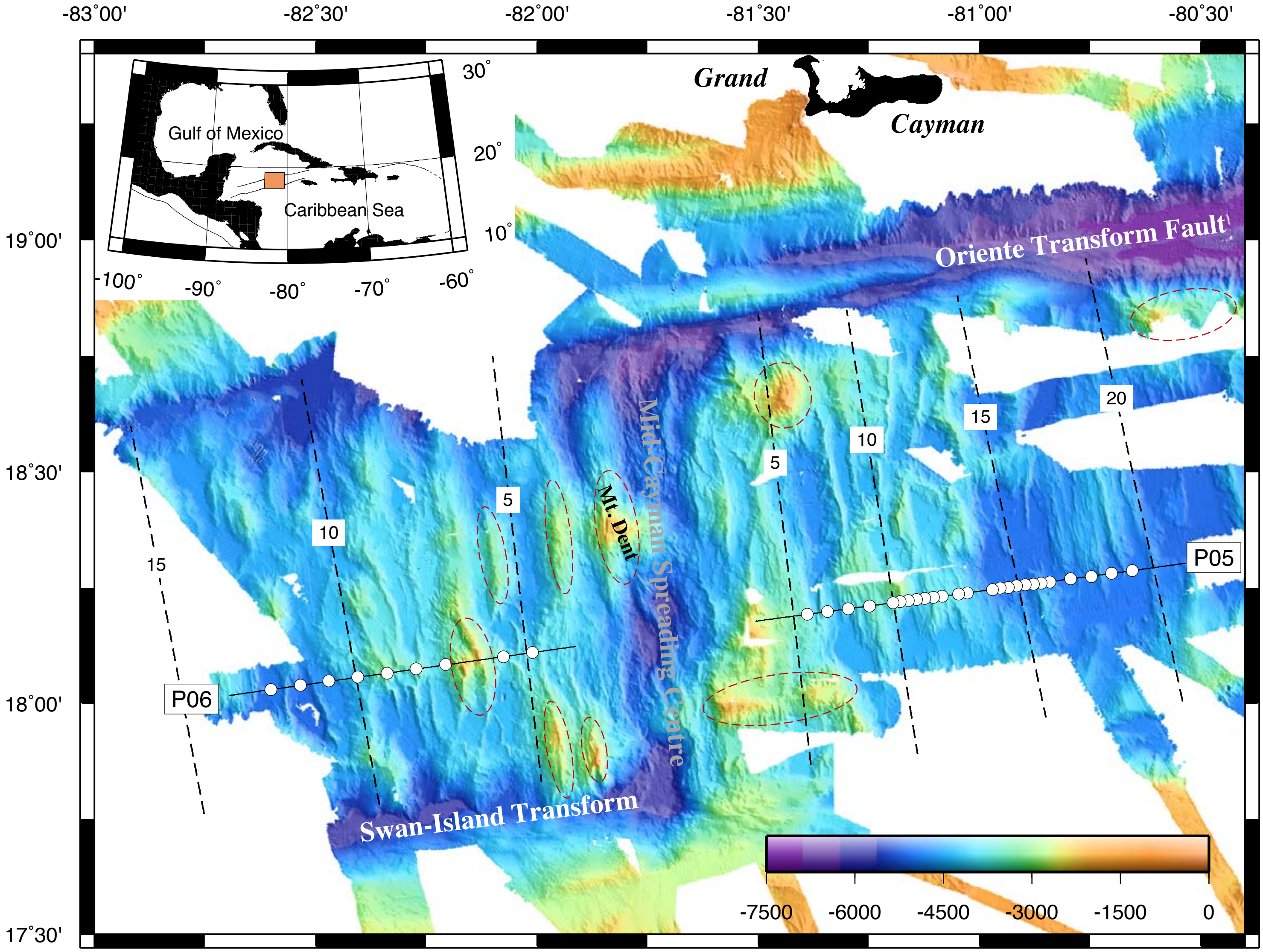

-83°00'
-82°30'
-82°00'
-81°30'
-81°00'
-80°30'
19°00'
18°30'
18°00'
17°30'
Gulf of Mexico
Caribbean Sea
30°
20°
10°
-100°
-90°
-80°
-70°
-60°
Grand
Cayman
Oriente Transform Fault
Mid-Cayman Spreading Centre
Mt. Dent
Swan-Island Transform
P05
P06
15
10
5
5
10
15
20
-7500
-6000
-4500
-3000
-1500
0

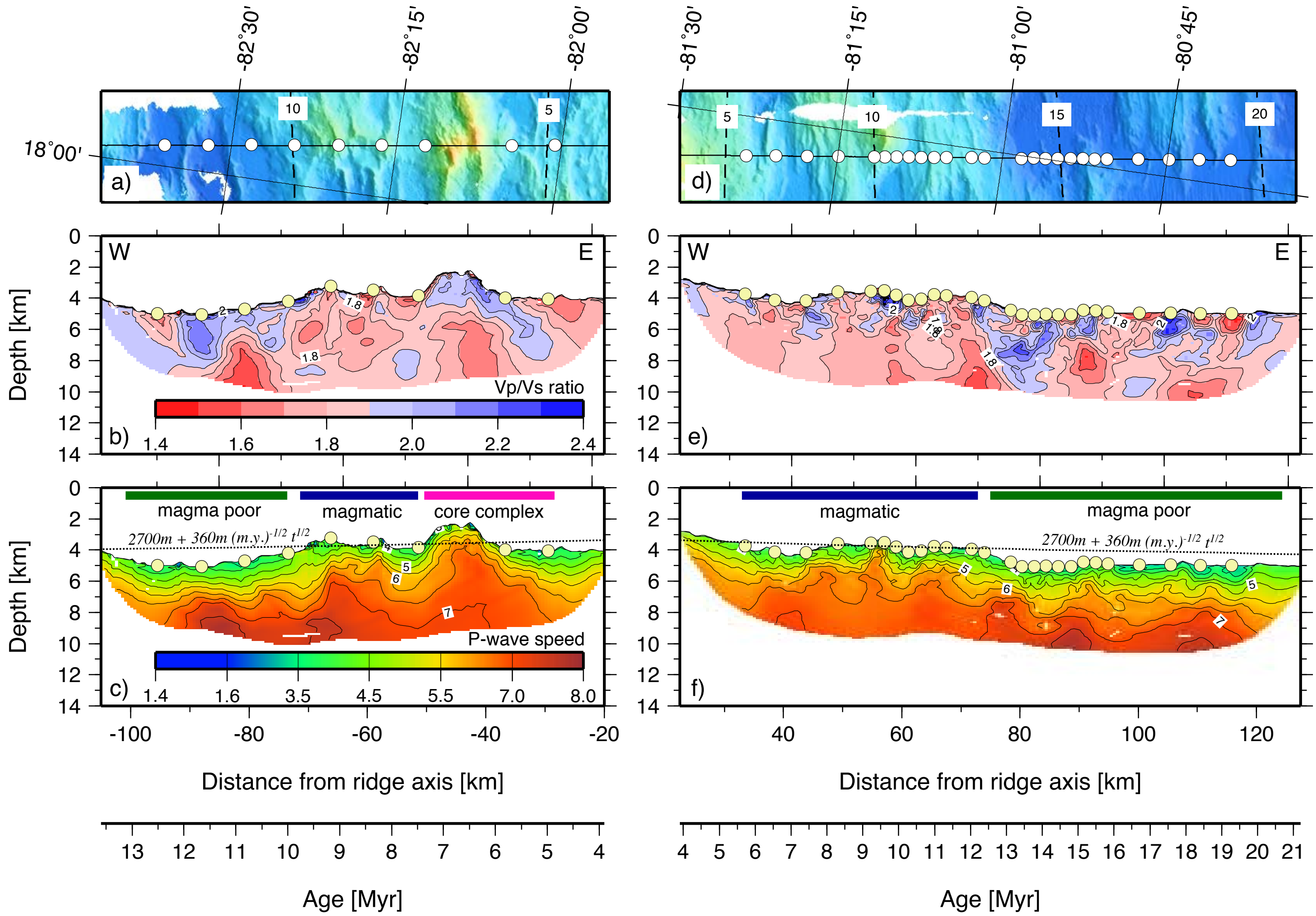

-82°30'
-82°15'
-82°00'
18°00'
10
5
a)
-81°30'
-81°15'
-81°00'
-80°45'
5
10
15
20
d)
W
E
Depth [km]
Vp/Vs ratio
1.4 1.6 1.8 2.0 2.2 2.4
b)
e)
magma poor
magmatic
core complex
2700m + 360m (m.y.)^-1/2 t^1/2
P-wave speed
1.4 1.6 3.5 4.5 5.5 7.0 8.0
c)
f)
Distance from ridge axis [km]
Age [Myr]

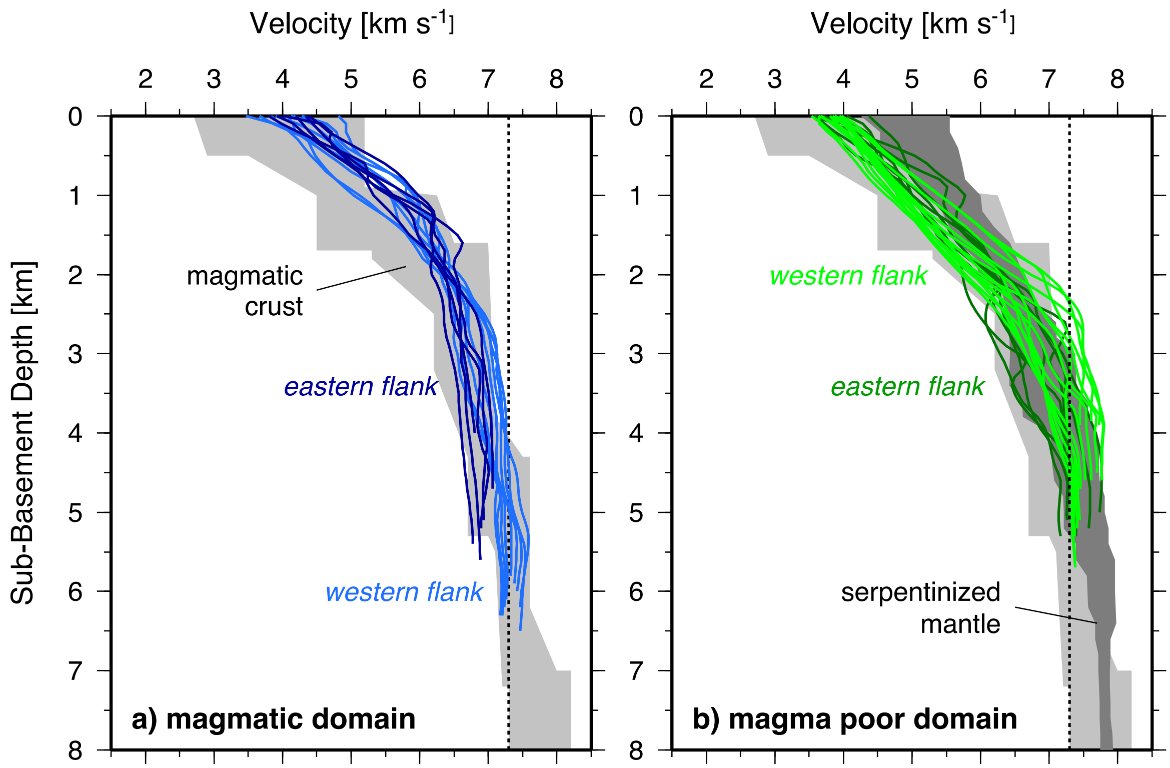

Velocity [km s-1]
2
3
4
5
6
7
8
0
1
2
3
4
5
6
7
8
Sub-Basement Depth [km]
magmatic
crust
eastern flank
western flank
a) magmatic domain
Velocity [km s-1]
western flank
eastern flank
serpentinized
mantle
b) magma poor domain

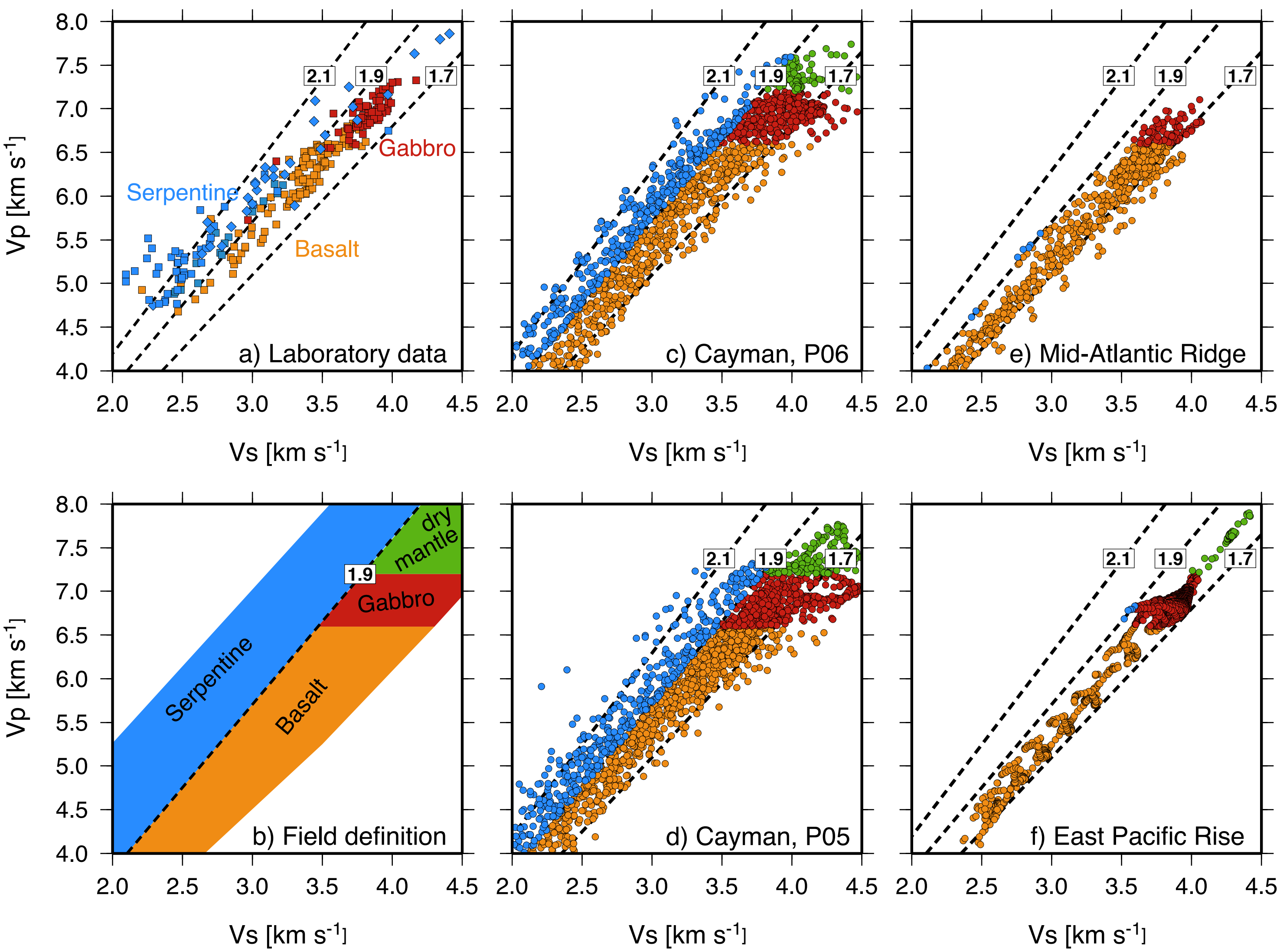

a) Laboratory data
b) Field definition
c) Cayman, P06
d) Cayman, P05
e) Mid-Atlantic Ridge
f) East Pacific Rise
Serpentine
Basalt
Gabbro
dry mantle
2.1
1.9
1.7
Vp [km s-1]
Vs [km s-1]

Supplementary Information Figure 1 | Data example from the eastern ridge flank. Reduced record section of seismic station no. 519 from profile P05.

Supplementary Information Figure 2 | Data example from the western ridge flank. Reduced record section of seismic station no. 608 from profile P06.

Supplementary Information Figure 3 | Results and associated errors of P05. a) Average P-wave velocity model derived from Monte Carlo inversion of 100 input models, b) average S-wave velocity model derived from Monte Carlo inversion of 100 input models, c) rms error associated with the P-wave analysis, d) rms error associated with the S-wave analysis, e) ray coverage of the P-wave model as expressed by the derivative weight sum (DWS)[39], f) ray coverage of the S-wave model as expressed by the DWS, g) average of Vp/Vs ratio obtained from 100 random combinations of P-wave and S-wave models, and h) rms error associated with the Vp/Vs ratio.

Supplementary Information Figure 4 | Results and associated errors of P06. a) Average P-wave velocity model derived from Monte Carlo inversion of 100 input models, b) average S-wave velocity model derived from Monte Carlo inversion of 100 input models, c) rms error associated with the P-wave analysis, d) rms error associated with the S-wave analysis, e) ray coverage of the P-wave model as expressed by the derivative weight sum (DWS)[39], f) ray coverage of the S-wave model as expressed by the DWS, g) average of Vp/Vs ratio obtained from 100 random combinations of P-wave and S-wave models, and h) rms error associated with the Vp/Vs ratio.

Supplementary Information Figure 5 | Results from gravity modelling. a) Bathymetry, b) satellite-derived gravity field[50] c) unfiltered shipboard gravity data compared to satellite-derived gravity, d) key iso-velocity contours used to guide gravity modelling, e) seismic velocity models at P06 (left) and P05 (right), f) density model derived from seismic velocity data, and g) fit of the calculated to the recorded gravity field.

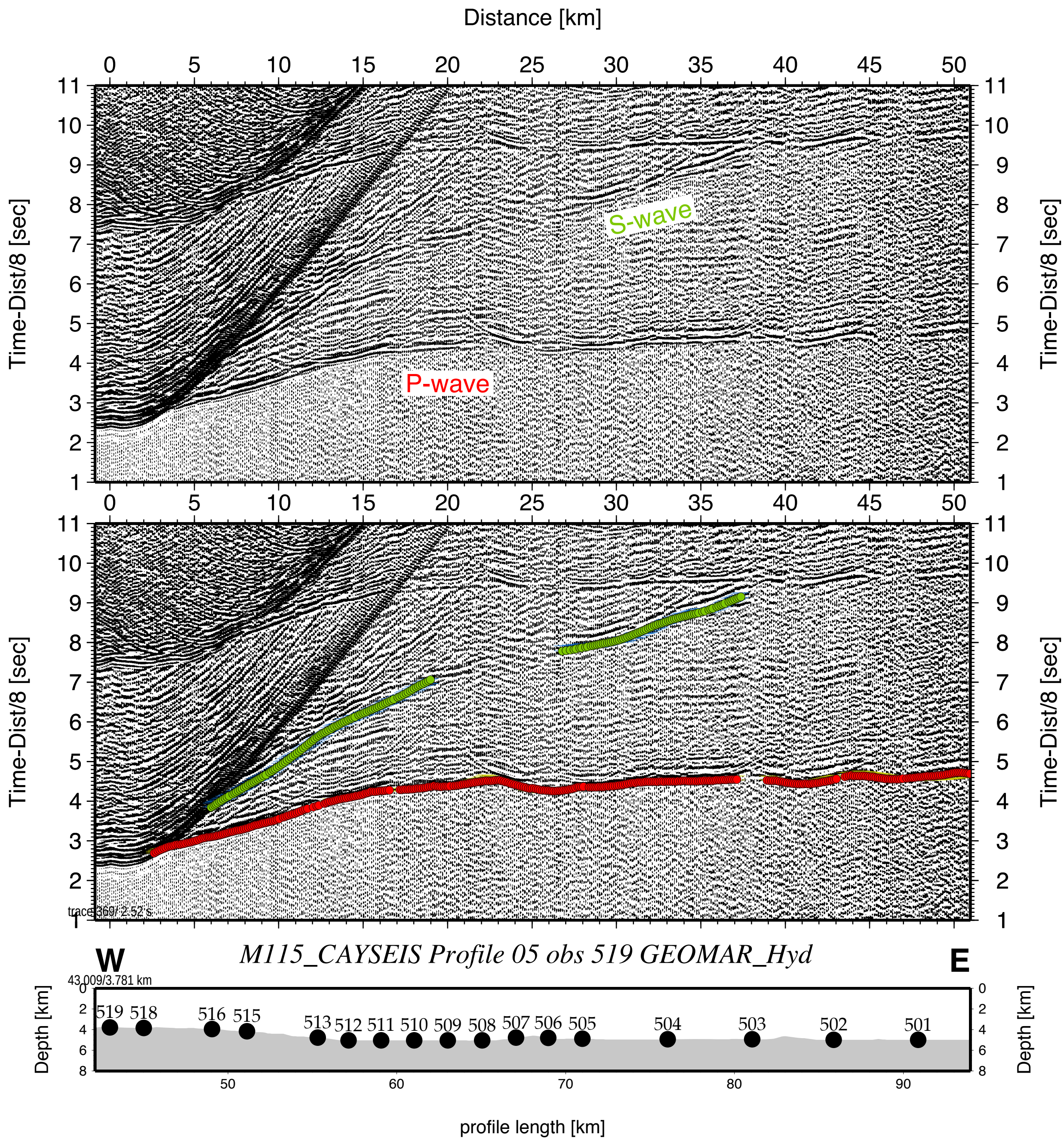
Distance [km]
Time-Dist/8 [sec]
S-wave
P-wave
trace 369/ 2.52 s
W
M115_CAYSEIS Profile 05 obs 519 GEOMAR_Hyd
E
43.009/3.781 km
Depth [km]
519 518 516 515 513 512 511 510 509 508 507 506 505 504 503 502 501
profile length [km]

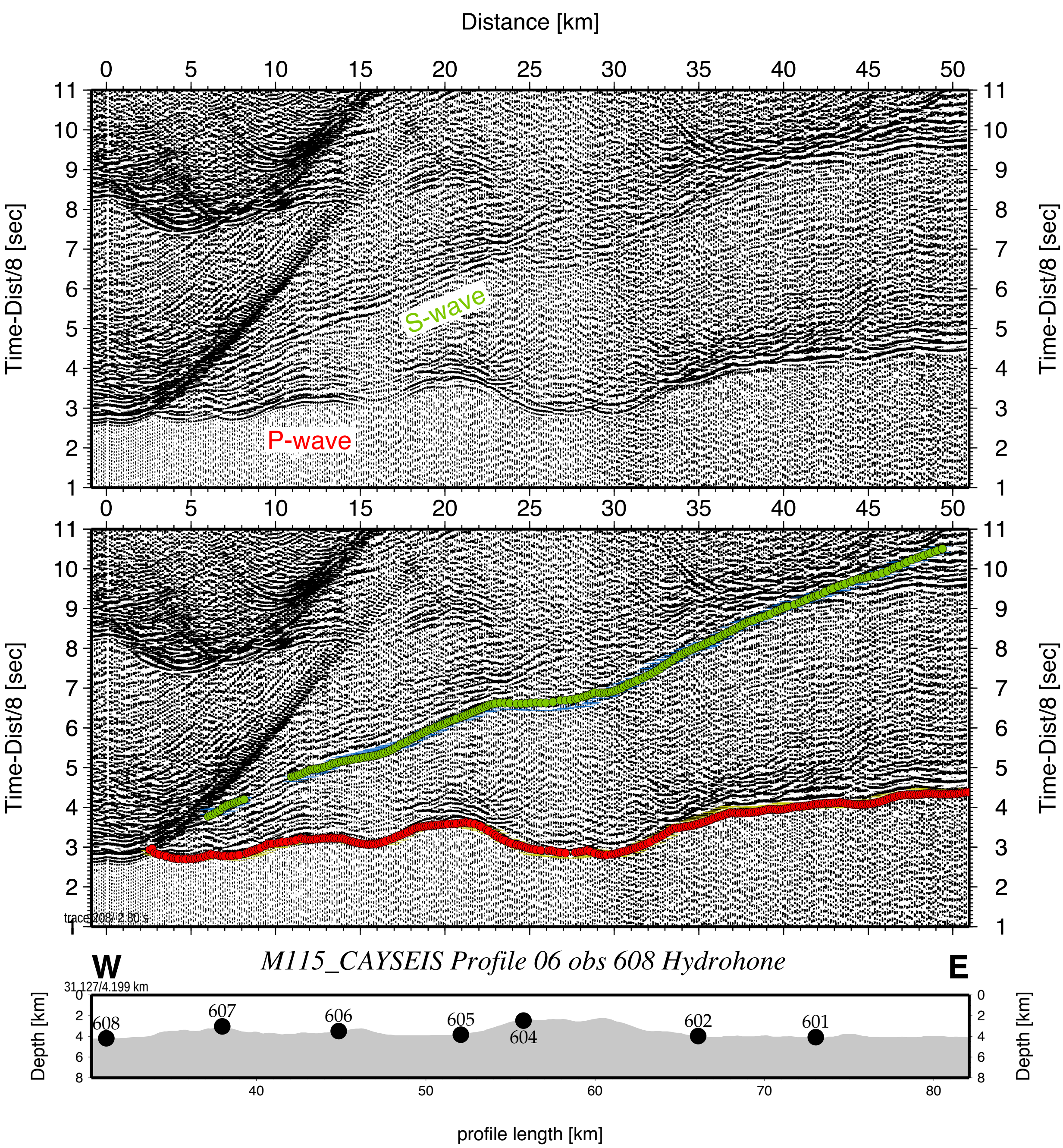
Distance [km]
Time-Dist/8 [sec]
S-wave
P-wave
trace 208/ 2.80 s
W
M115_CAYSEIS Profile 06 obs 608 Hydrohone
E
31.127/4.199 km
Depth [km]
608
607
606
605
604
602
601
profile length [km]

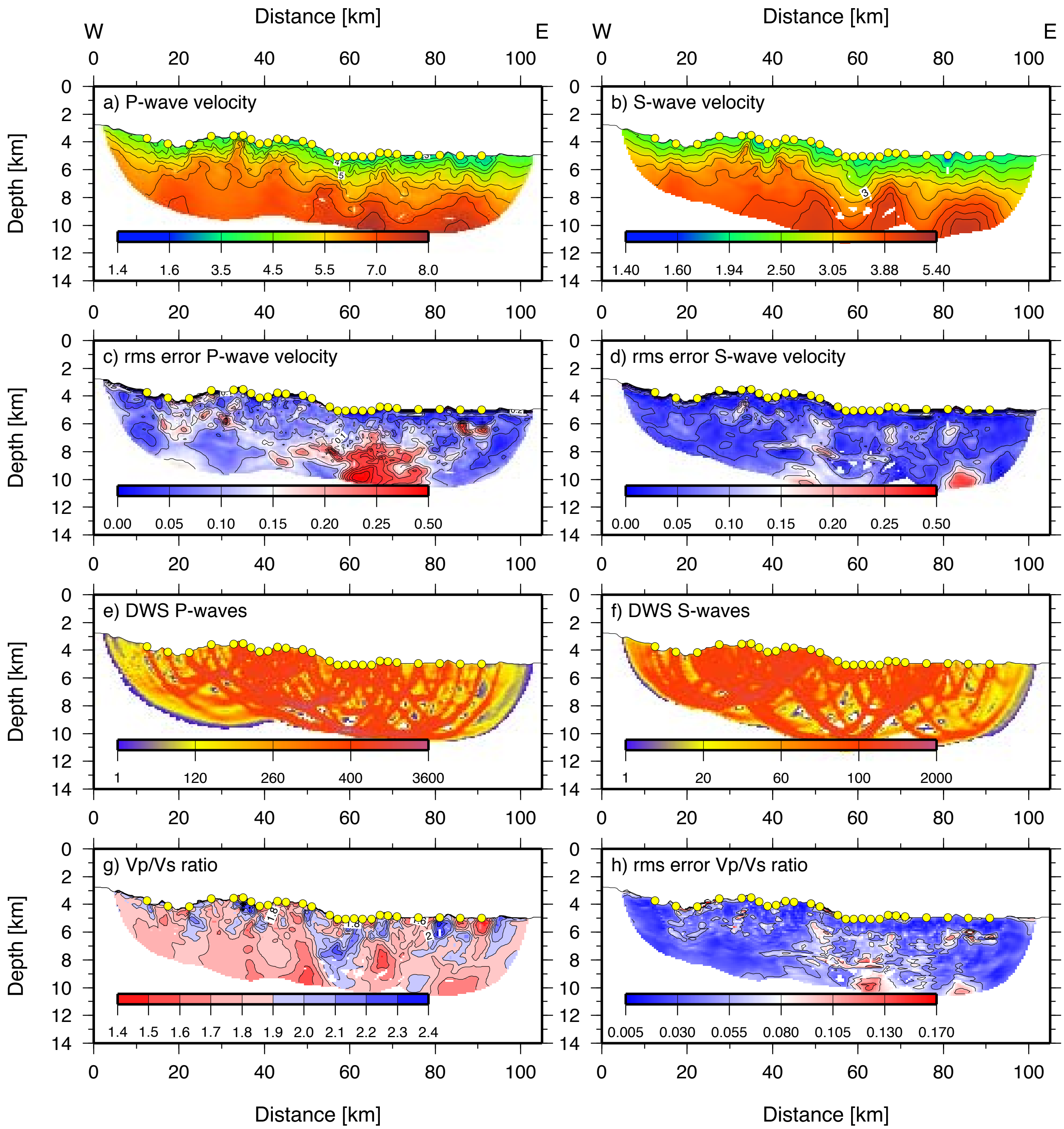

Distance [km]
W
E
Depth [km]
a) P-wave velocity
1.4 1.6 3.5 4.5 5.5 7.0 8.0
b) S-wave velocity
1.40 1.60 1.94 2.50 3.05 3.88 5.40
c) rms error P-wave velocity
0.00 0.05 0.10 0.15 0.20 0.25 0.50
d) rms error S-wave velocity
0.00 0.05 0.10 0.15 0.20 0.25 0.50
e) DWS P-waves
1 120 260 400 3600
f) DWS S-waves
1 20 60 100 2000
g) Vp/Vs ratio
1.4 1.5 1.6 1.7 1.8 1.9 2.0 2.1 2.2 2.3 2.4
h) rms error Vp/Vs ratio
0.005 0.030 0.055 0.080 0.105 0.130 0.170

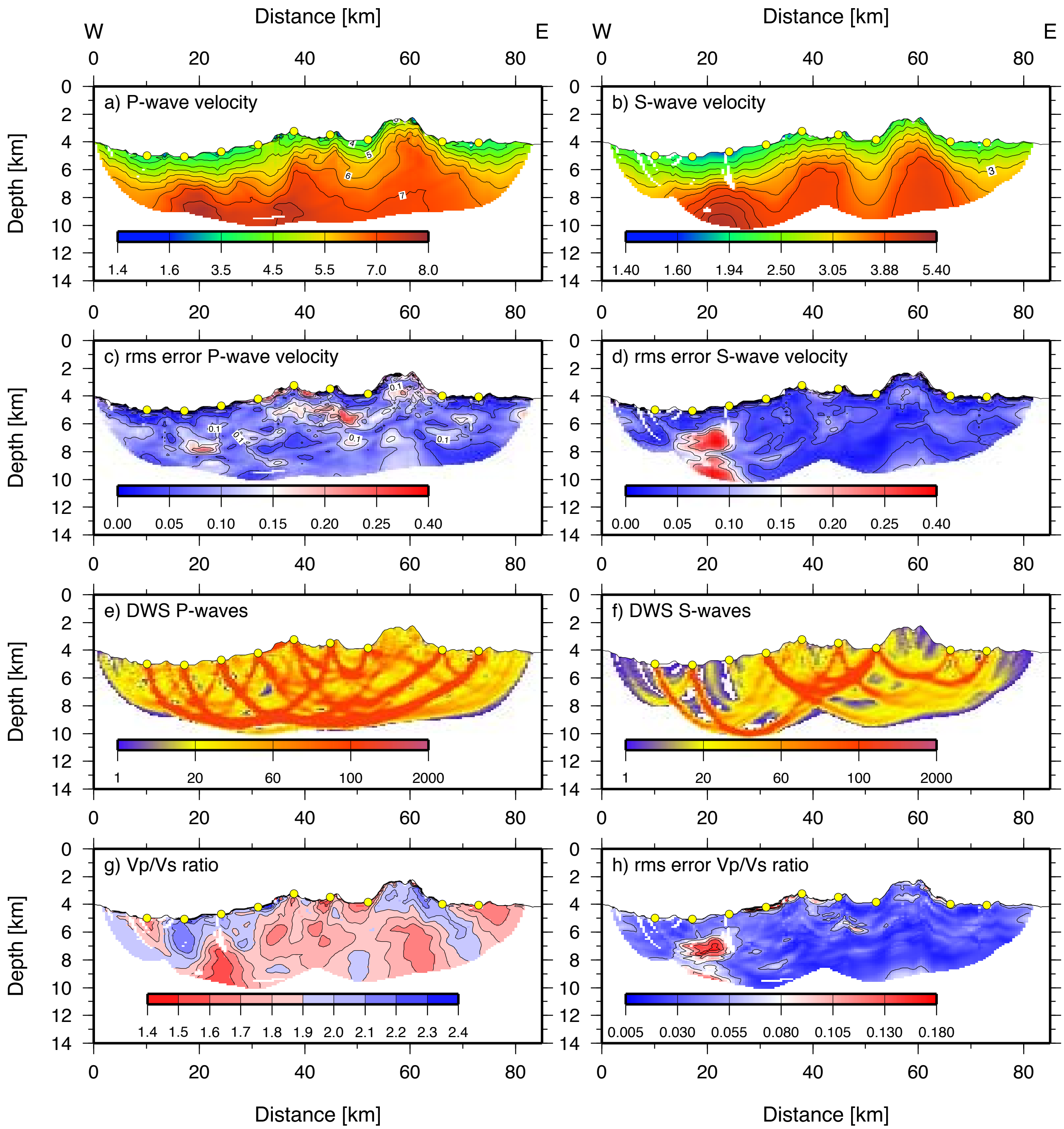
Distance [km]
W
E
Depth [km]
a) P-wave velocity
1.4 1.6 3.5 4.5 5.5 7.0 8.0
b) S-wave velocity
1.40 1.60 1.94 2.50 3.05 3.88 5.40
c) rms error P-wave velocity
0.00 0.05 0.10 0.15 0.20 0.25 0.40
d) rms error S-wave velocity
0.00 0.05 0.10 0.15 0.20 0.25 0.40
e) DWS P-waves
1 20 60 100 2000
f) DWS S-waves
1 20 60 100 2000
g) Vp/Vs ratio
1.4 1.5 1.6 1.7 1.8 1.9 2.0 2.1 2.2 2.3 2.4
h) rms error Vp/Vs ratio
0.005 0.030 0.055 0.080 0.105 0.130 0.180
Distance [km]

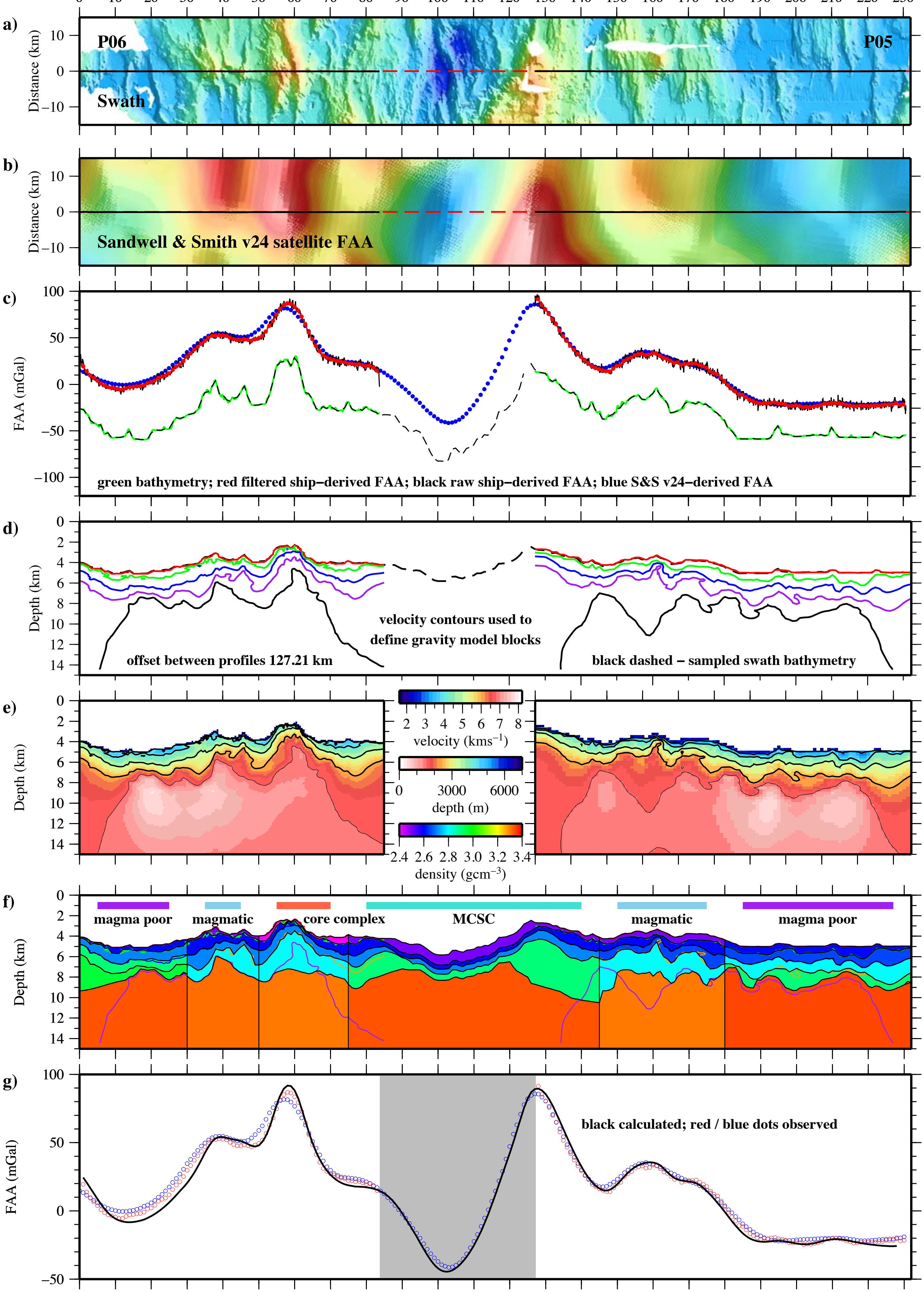
a)
P06
P05
Swath
Distance (km)
b)
Sandwell & Smith v24 satellite FAA
c)
FAA (mGal)
Depth (m)
green bathymetry; red filtered ship−derived FAA; black raw ship−derived FAA; blue S&S v24−derived FAA
d)
Depth (km)
velocity contours used to define gravity model blocks
offset between profiles 127.21 km
black dashed − sampled swath bathymetry
e)
velocity (kms^{-1})
depth (m)
density (gcm^{-3})
f)
magma poor
magmatic
core complex
MCSC
magmatic
magma poor
g)
black calculated; red / blue dots observed